Investigation of viscous coupling effects in three-phase flow by lattice Boltzmann direct simulation and machine learning technique

Fei Jiang[a,b,c,*], Jianhui Yang[d], Edo Boek[e], Takeshi Tsuji[c,f]

[a]*Department of Mechanical Engineering, Yamaguchi University, Ube, Japan*
[b]*Blue energy center for SGE technology (BEST), Yamaguchi University, Ube, Japan*
[c]*International Institute for Carbon-Neutral Energy Research (WPI-I2CNER), Kyushu University, Fukuoka, Japan*
[d]*Geoscience Research Centre, TOTAL E & P UK Limited, Westhill, UK*
[e]*Division of Chemical Engineering & Renewable Energy, School of Engineering and Materials Science, Queen Mary University of London, London, UK*
[f]*Department of Earth Resources Engineering, Kyushu University, Fukuoka, Japan*

Abstract

The momentum transfer across fluid interfaces in multi-phase flow leads to a non-negligible viscous coupling effect. In this study, we use the lattice Boltzmann method (LBM) as a direct simulator to solve the three-phase flow at pore scale. The viscous coupling effects are investigated for various fluid configurations in simple pore geometries with different conditions in terms of saturation, wettability and viscosity ratio. It is found that the viscous coupling effect can be significant for certain configurations. A parametric modification factor for conventional three-phase conductance model is then proposed to estimate the viscous coupling effect. The modification factor as a function of viscosity ratios can be easily incorporated into existing pore network model (PNM) to eliminate errors from viscous coupling effect. Moreover, an elegant approach using machine learning technique is proposed to predict the multi-phase permeability by a trained Artificial Neural Network (ANN) from the direct simulation database. Such data-driven approach can be extended to develop a more sophisticated PNM for a better prediction of transport properties taking account of the viscous coupling effects.

*Corresponding author.
E-mail address: fjiang@yamaguchi-u.ac.jp

Keywords: Viscous coupling effect, multiphase flow, Lattice Boltzmann method, Porous media

1. Introduction

The pore-scale behavior of multiphase flow in porous media is essential for many applications, including oil recovery, carbon dioxide storage, and fuel cell optimization [1]. The three-phase flow behavior is of great importance in petroleum engineering due to the fact that many enhanced oil recovery (EOR) processes such as water-alternating-gas injection, steamflooding, etc. rely on the complicated phenomena of three-phase systems (oil, water and gas).

Modeling such multiphase flow at the porous scale is required to investigate detailed displacement mechanisms and transport behaviors. Various pore scale models have been developed to predict constitutive properties such as the relationship between permeability and the fluid saturation and the relationship between capillary pressure and the saturation[1]. The pore scale models can be categorized as indirect and direct methods. In the indirect method, the pore spaces are represented by simple sphere or cube geometries which are connected by throats with idealized shapes[2, 3]. Pore Network Modeling (PNM)[4, 5, 6, 3] is a typical indirect method which solves simplified transport equations on idealized pore geometries. Several algorithms were proposed to generate proxy pore-network models for 3D pore structure reconstructed from computed tomography images of reservoir rocks[7, 8]. Pore-network models have been used as a popular tool because of their efficiency and ability to quickly estimate transport properties such as the relative permeability which is extremely time consuming to measure experimentally. Patzek et al. [9] successfully simulated drainage and imbibition processes in pore-network models to predict multiphase flow properties. Three-phase pore network modeling has also been developed decades ago[10, 11, 12]. The predictive capabilities of network models have improved such that they can also be used to calculate three-phase relative permeability [13, 14]. The limitation of pore-network modeling resided in the inaccuracy of empirical models and the extraction of the pore spaces. Due to such simplification of flow processes and pore-space geometry, some important phenomena such as viscous coupling has been neglected[15, 16, 17]. The viscous coupling effect is usually important as it influences the prediction accuracy of relative permeability

curves [18, 16, 17]. The experimental data also showed the importance of the viscous coupling during three-phase flow in porous media [19, 20]. Dehghanpour et al. [19] measured the relative permeabilites of three-phase flow, and the observed flow coupling effect between water and oil is even stronger in three-phase flow than two-phase flow.

On the other hand, the use of direct methods implies that we solve the physical governing equations on the exact realistic geometry of the porous media at the pore scale. Therefore, it is possible to accurately capture the missing physical phenomena in PNM if the correct governing equations are selected and solved properly. Numerical schemes such as finite element [21, 22], finite volume[23, 24, 25], and lattice Boltzmann methods (LBM) [26, 27, 28, 29, 30, 31, 32, 33, 34, 35] have been used for the direct simulations. The LBM is the most popular method for capturing the multiphase fluid transport in porous media because of its simplicity in treating complex pore geometry coupled with interfacial phenomena and thermodynamics[36, 37, 27, 38, 39, 29, 40, 32]. However, the LBM as well as other direct simulation approach are extremely computationally expensive. This will cause some difficulties to compute properties at large REV (representative elementary volume) sizes of rock samples at the mm to cm scale. Parallel computation techniques have been comprehensively used to improve the computational efficiency and scalability [41, 42, 43]. However, such simulations still require large computational resources such as super computers. As a more practical and applicable solution, the combination of direct numerical simulation and pore-network modeling is considered to be a good approach for multiphase flow properties prediction.

In this work, we developed an improved conductance model for the PNM using data derived from direct pore-scale LBM simulations. The improved model is proposed to incorporate important viscous coupling effects for multiphase flow conditions. The viscous coupling effects, which are neglected in PNMs, have been proven to have a substantial influence on multiphase flow processes. [44, 36, 16, 17]. Li et al. [44] found that the interfacial area between fluids strongly affects the permeability, indicating that the common extension of Darcy's Law cannot capture flow properties accurately. Huang and Lu [36] investigated viscous coupling effects by simulating co- and countercurrent steady-state two-phase flow and found that viscous coupling effects are strongly related to the saturation distribution. Xie et al. [16] proposed an improved empirical function by introducing a correction factor to include the viscous coupling effect into PNM and achieved better predictions of relative

permeability. Shams et al. [17] presented a simple parametric model for the hydraulic conductance as a function of the geometry and viscosity ratio to account for viscous coupling effects. However, most of all these models are developed for two-phase flow frameworks. Regarding the conductance model of the three-phase flow, Al-Futaisi and Patzek [45] used a finite-element method to solve the three-phase creeping flow in angular capillaries and adopted a regression method to model hydraulic conductance. However, they ignored the continuity conditions of velocity and shear stress along the interfaces, and a prescribed interface shape is required. To consider the momentum transfer at the interface, we use the LBM to simulate three-phase flow at the pore scale with various geometric parameters and viscosity ratios, because LBM is able to naturally satisfy the continuity conditions of velocity and shear stress and is more flexible in handling the contact angles. The dependence of viscous coupling effects on these parameters is then investigated. Furthermore, an improved empirical correlation for the conductance is developed by introducing a modification factor as a function of viscosity ratio in the conventional three-phase conductance model [46] incorporating the viscous coupling effect. Finally, machine learning techniques have been used to predict the permeability of three-phase flow considering the viscous coupling effect in pore throat by a trained Artificial Neural Network (ANN). We use the LB direction simulations to generate a database with a set of input parameters including the viscosity ratios for training. These two newly-proposed models can be incorporated into PNM for a better prediction of transport properties with the consideration of viscous coupling effects.

2. Methodology

2.1. Empirical equations of pore-network model

In pore-network models, the conductance g_a is the key parameter to compute the absolute and relative permeability [15]. Using the conductance g_a, the local flow rate $q_{ij,a}$ (Fig. 1) of the phase a between two connected pores i and j can be given by Darcy's law (Fig. 1):

$$q_{ij,a} = g_{ij,a} \nabla P_{ij} \tag{1}$$

where ∇P_{ij} is the pressure gradient of fluid a between adjacent pores i and j (Fig. 1). Since the exact analytic solution for conductance is generally unknown, several empirical expressions have been developed for different

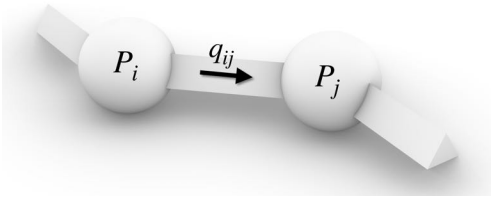

Figure 1: Pore-network model

fluid configurations and different pore geometries [46]. Depending on the number of phases coexisting in the pore, the conductance g_a is determined accordingly. The single-phase conductance is given by

$$g = \lambda \frac{A^2 G}{\mu} \tag{2}$$

in which, parameter λ is 0.5, 0.6 and 0.5623 for circular, triangular and square elements respectively [16]. G is the shape factor, μ is the dynamic viscosity and A is the cross-sectional area.

For two-phase flow, the conductance of each phase must be calculated depending on the fluid occupation. For fluids occupying the corner and layer area, Valvatne and Blunt [15] developed empirical expressions as

$$g_c = C \frac{A_c^2 G_c}{\mu_c} \tag{3}$$

$$g_l = \frac{b_0^4 \widetilde{g}_l}{\mu_l} \tag{4}$$

where subscripts c and l represent the corner and layer configurations respectively. A_c is the area of the corner phase and parameters C and G_c are determined by the corner fluid geometry, while b_0 and $\widetilde{g}_l$ are related to the layer fluid geometry.

For three-phase flow, Hui and Blunt [11] proposed the following expressions to compute the conductance of wetting (corner) and spreading (sandwiched) layers for a three phase coexisting pore corner (Fig. 2). The conductance of the corner phase can be estimated by:

$$g^c = \frac{A_c^2 (1 - \sin\alpha)^2 (\varphi_2 \cos\theta - \varphi_1)\varphi_3^2}{12\mu \sin^2\alpha (1 - \varphi_3)^2 (\varphi_2 + f\varphi_1)^2} \quad \theta_I \leq \frac{\pi}{2} - \alpha \tag{5}$$

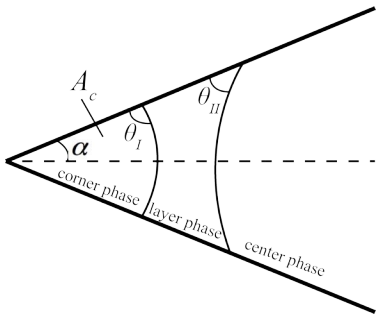

Figure 2: A sandwich corner of the three-phase system

$$g^c = \frac{A_c^2 \tan\alpha(1-\sin\alpha)^2\varphi_3^2}{12\mu \sin^2\alpha(1-\varphi_3)(1+f\varphi_3)^2} \quad \theta_I > \frac{\pi}{2} - \alpha \tag{6}$$

$$\varphi_1 = (\frac{\pi}{2} - \alpha - \theta) \tag{7}$$

$$\varphi_2 = \cot\alpha\cos\theta - \sin\theta \tag{8}$$

$$\varphi_3 = (\frac{\pi}{2} - \alpha)\tan\alpha \tag{9}$$

where, $\theta = \theta_I$ and α is the corner angle. The conductance of the sandwiched phase can be estimated by:

$$g^l = \frac{A_1^3(1-\sin\alpha)^2\tan\alpha\varphi_3^2}{12\mu A_c \sin^2\alpha(1-\varphi_3)\left[1+f_1\varphi_3-(1-f_2\varphi_3)\sqrt{\frac{A_2}{A_{cl}}}\right]^2} \tag{10}$$

where, the parameters A_1 and A_2 are the areas of sandwiched phase and corner phase, respectively. A_{cl} is a summation of areas of corner and sandwiched phase.

The empirical equation of conductance for two-phase flow (Eq. (3) and Eq. (4)) completely neglect the viscous coupling which means flow in each phase is independent of the other phase. Xie et al. [16] proposed a modification factor correcting the original empirical equations to include the viscous coupling effect. Here, in the case of three-phase flow, there is a parameter f in Eq.(6) which implicitly reflects the viscous coupling effect between each phase. $f = 1$ represents a no-flow boundary condition (completely neglecting the viscous coupling effect), while $f = 0$ represents a free-slip boundary

condition. No-flow boundary condition means that the interface is treated as a solid boundary and the velocity of each phase at the interface is forced to be zero (no-slip). Free-slip boundary condition indicates that the interface is treated as a perfectly lubricated boundary (fluid can slip freely at the interface). Both of these two conditions are unrealistic, because continuity of velocity and shear stress along the interface must be satisfied to consider the momentum exchange at the interface. For the equation of the sandwiched phase's conductance (Eq. (10)), two parameters f_1 and f_2 are involved because there are two interfaces: layer-center interface and corner-layer interface. To quantify the viscous coupling effect, instead of using the constant value for the parameters f, f_1 and f_2, we try to develop a function of viscosities of the three phases by determining the values of f, f_1 and f_2 in order to improve the accuracy of empirical equations.

2.2. Direct pore-scale simulation method for three-phase flow

To develop an improved conductance model, we use direct pore-scale simulation method to provide the details of three-phase flow. Then we could derive similar modification factors [16] from the detailed direct numerical simulation results. Here, we adopt a color-gradient three-phase LB model [38, 29, 47] as the direct pore-scale flow solver. In this method, the three-phase flow is solved in an integrated manner, and the shape of the interfaces is determined by the fundamental physical parameters (e.g. wettability and surface tension). In LBM, particle distribution functions (PDF) $f_i^k(\mathbf{x}, t)$ are introduced to represent three different fluids where i and k denote the velocity direction and phase respectively. The evolution of $f_i^k(\mathbf{x}, t)$ is governed by the following LB equation:

$$f_i^k\left(\mathbf{x} + \mathbf{e}_i\delta t, t + \delta t\right) = f_i^k(\mathbf{x}, t) + \Omega_i^k(\mathbf{x}, t) \tag{11}$$

where $\mathbf{e}_i$ is the lattice velocity in the ith direction, δt is the time step, and Ω_i^k is the collision operator:

$$\Omega_i^k = \left(\Omega_i^k\right)^{(3)}\left[\left(\Omega_i^k\right)^{(1)} + \left(\Omega_i^k\right)^{(2)}\right] \tag{12}$$

where $\left(\Omega_i^k\right)^{(1)}$ is the single-phase collision operator, $\left(\Omega_i^k\right)^{(2)}$ is the multiphase collision operator for perturbation, which generates interfacial tensions, and $\left(\Omega_i^k\right)^{(3)}$ is the multiphase collision operator for the phase segregation. Those collision operators are given as:

$$\left(\Omega_i^k\right)^{(1)}\left(f_i^k\right) = f_i^k - \mathbf{M}^{-1}\mathbf{S}\mathbf{M}\left(f_i^k - f_i^{k,eq}\right) \tag{13}$$

$$\left(\Omega_i^k\right)^{(2)}\left(f_i^k\right) = f_i^k + \sum_{l,l\neq k}\frac{A_{kl}}{2}\left|\mathbf{G}_{kl}\right|\left[W_i\frac{\left(\mathbf{G}_{kl}\cdot\mathbf{e}_i\right)^2}{\left|\mathbf{G}_{kl}\right|^2} - B_i\right] \tag{14}$$

$$\left(\Omega_i^k\right)^{(3)}\left(f_i^k\right) = \frac{\rho_k}{\rho}f_i^* + \sum_{i,k\neq k}\beta_{kl}\frac{\rho_k\rho_l}{\rho^2}\cos\left(\varphi_i^{kl}\right)f_i^{eq}\left(\rho,0\right) \tag{15}$$

To improve the numerical stability and remove the uncertainty due to viscosity-dependence [48], the multiple-relaxation-time (MRT) operator [49] of the single-phase LB model is adopted here as the first sub-operator $\left(\Omega_i^k\right)^{(1)}$. The $\mathbf{M}$ matrix transforms the particle distributions into moment space which is given by Tolke et al. [50], and then distribution functions are relaxed towards a local equilibrium f_i^{eq} with a diagonal matrix of relaxation coefficients $\mathbf{S}$. The equilibrium f_i^{eq} is a function of density and velocity, which can be found in [51, 29]. The relaxation coefficients $\mathbf{S}$ are determined according to the fluid's kinematic viscosity ν and numerical stability considerations [52]. In Eq .(14), W_i is the weights depending on the lattice type and B_i is the parameter related to the lattice speed. In this paper, we choose D3Q19 (three-dimensional 19-velocity) lattice with $B_0 = -1/3$, $W_0 = 1/3$, $W_{1-6} = B_{1-6} = 1/18$, and $W_{7-18} = B_{7-18} = 1/36$ [53].

In the second perturbation operator $\left(\Omega_i^k\right)^{(2)}\left(f_i^k\right)$, A_{kl} is related to the interfacial tension between $k-l$ fluid interfaces. $\mathbf{G}_{kl}$ is the color gradient indicating the normal direction of $k-l$ fluid interfaces, which can be calculated from the density field as [47]:

$$\mathbf{G}_{kl} = \frac{\rho_l}{\rho}\nabla\left(\frac{\rho_k}{\rho}\right) - \frac{\rho_k}{\rho}\nabla\left(\frac{\rho_l}{\rho}\right) \tag{16}$$

In the above equation, the gradient operator for an arbitrary variable ϕ is approximated by [53, 34, 54] :

$$\nabla\phi\left(\mathbf{x},t\right) = \frac{3}{c^2}\sum_i w_i\mathbf{e}_i\phi\left(\mathbf{x}+\mathbf{e}_i\delta t,t\right) \tag{17}$$

To promote phase segregation and maintain a sharp interface [55], a third recoloring operator $\left(\Omega_i^k\right)^{(3)}\left(f_i^k\right)$ has to be applied. In the recolor operator, f_i^* denotes the post-perturbation value of the total particle distribution function,

and β_{kl} is a parameter [56] controlling the thickness of the $k-l$ interface taking a value of between 0 and 1.The β_{kl} is set to be 0.8 for all the simulations in this study, and the interface thickness is around 5 lattices. When the viscosities of the fluids are different, an interpolation is applied to calculate the viscosities in the interfacial region [47]. As a result, the smooth transition of interfacial viscosities can be obtained and the continuity conditions of velocity and shear stress at the interface are naturally ensured. φ_i^{kl} indicates the angle between the color gradient $\mathbf{G}_{kl}$ and the lattice direction vector $\mathbf{e}_i$. The $f_i^{eq}(\rho, 0)$ is the equilibrium function calculated with a zero velocity. Finally, the macroscopic flow properties including density ρ and velocity $\mathbf{u}$ can be calculated as :

$$\rho = \sum_k \rho_k,\ \rho_k = \sum_i f_i^k,\ \rho\mathbf{u} = \sum_i \sum_k f_i^k \mathbf{e}_i \tag{18}$$

2.3. Validation

2.3.1. Three-phase co-current flow between parallel plates

For immiscible three-phase flows in porous media, a typical scenario is that the wetting fluid attaches and moves along the solid surface forming a wetting layer. Therefore, we first investigated a layered three-phase co-current flow in a straight channel (Fig. 3) to validate the numerical method and confirm the viscous coupling effects. The fluid 1 flows in the center, while fluid 3 flows along the upper and lower plates. The sandwiched fluid 2 lays in between fluid 1 and fluid 3. The distance between the upper and lower plates is $2H$. The coordinates of the interface between fluid 1 and 2 are $\pm a$, while the coordinates of the interface between fluid 2 and 3 are $\pm b$. The governing equations of fluid flow for each phase are given by

$$\mu_l \nabla^2 u_l = \nabla P_l, \tag{19}$$

where subscript l represents the different phase ($l = 1, 2, 3$), μ is the viscosity and P is the pressure. The $u_l(y)$ are the velocities of each phase. The boundary conditions are

$$u_1|_{y=a} = u_2|_{y=a},\ u_2|_{y=b} = u_3|_{y=b},\ u_3|_{y=H} = 0 \tag{20}$$

$$\left.\frac{\partial u_1}{\partial y}\right|_{y=0} = 0,\ \mu_1 \left.\frac{\partial u_1}{\partial y}\right|_{y=a} = \mu_2 \left.\frac{\partial u_2}{\partial y}\right|_{y=a},\ \mu_2 \left.\frac{\partial u_2}{\partial y}\right|_{y=b} = \mu_3 \left.\frac{\partial u_3}{\partial y}\right|_{y=b} \tag{21}$$

The theoretical cross-sectional velocity distribution can be obtained by solving the above equations with the boundary conditions:

$$\begin{array}{rl} 0 \le y < a: & u_1 = A_1 y^2 + C_1 \\ a \le y < b: & u_2 = A_2 y^2 + B_2 y + C_2 \\ b \le y \le H: & u_3 = A_3 y^2 + B_3 y + C_3 \end{array} \tag{22}$$

where

$$A_1 = 0.5\nabla P_1/\mu_1,\ A_2 = 0.5\nabla P_2/\mu_2,\ A_3 = 0.5\nabla P_3/\mu_3, \tag{23}$$

$$B_2 = -2A_2 a + 2\frac{\mu_1}{\mu_2} A_1 a, \tag{24}$$

$$B_3 = -2A_3 b + \frac{\mu_2}{\mu_3}(2A_2 b + B_2), \tag{25}$$

$$C_3 = -A_3 H^2 - B_3 H, \tag{26}$$

$$C_2 = (A_3 - A_2)b^2 + (B_3 - B_2)b + C_3, \tag{27}$$

$$C_1 = (A_2 - A_1)a^2 + B_2 b + C_2, \tag{28}$$

The conductance of the three fluids can be calculated from the velocity distribution. It is clear that the velocity profile of each phase is correlated to the viscosity ratio (Eq. 22), which confirms the importance of the viscous coupling effect. The analytical solution is usually difficult to obtain for other types of complex configurations, therefore direct simulation by lattice Boltzmann multiphase model is adopted to address the viscous coupling effect for those complex configurations. Numerical simulation tests are performed by simulating this layered three-phase co-current flow. The computation domain is set as $100 \times 101 \times 20$ lattice sites. Periodic boundary conditions are applied on the x and z directions. Non-slip boundary conditions at the top and bottom solid wall in y direction are implemented by using the bounce-back scheme. For simplicity, the densities of the three phases are set to be identical. The surface tension σ is chosen to be 0.01 in lattice unit. A uniform pressure gradient along the flow direction ($\nabla P_1 = \nabla P_2 = \nabla P_3 = \nabla P$) is applied on the whole domain. In our simulation, a body force of 10^{-6} in

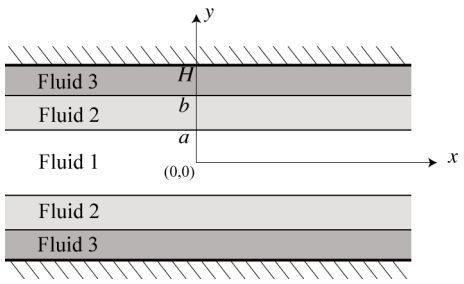

Figure 3: Concurrent immiscible three-phase flow in a channel.

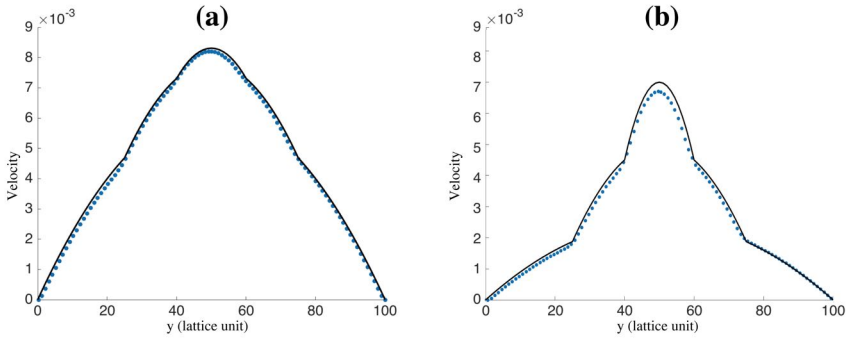

Figure 4: Comparison of cross-sectional velocity profile between theoretical solution (black line) and simulation results (blue dot) for the three-phase co-current flow with different viscosity ratio: (a) case I with $\mu_1 : \mu_2 : \mu_3 = 1 : 2 : 4$; (b) case II with $\mu_1 : \mu_2 : \mu_3 = 1 : 5 : 25$

lattice units is applied to mimic the pressure gradient. Two cases with different viscosity ratios are considered here: case I with $\mu_1 : \mu_2 : \mu_3 = 1 : 2 : 4$ and case II with $\mu_1 : \mu_2 : \mu_3 = 1 : 5 : 25$. After the systems reach the steady state, the velocity profiles along y axes are shown in Fig. 4. For case I, our simulation results showed a good agreement with the theoretical solution, while for case II the peak velocity of center-layer phase obtained from LBM is about 4.3% lower than that of analytical one. This small discrepancy may due to the large viscosity ratio. It has been reported that high viscosity ratio decreases the accuracy of the model [57]. These validation cases confirm the capability of our direct flow solver to account for the viscous coupling effect.

2.3.2. Viscous coupling effect on velocity distribution of triangular pore throat

To investigate the effect of the center layer's viscosity on the velocity distribution in the cross section of triangular pore throat, we performed

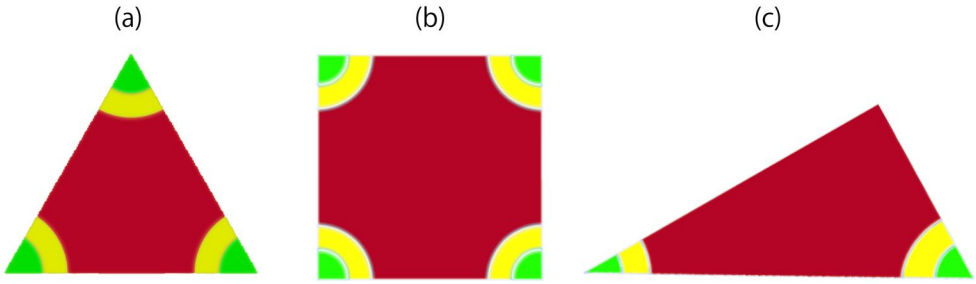

Figure 5: Three-phase fluid configurations (different color indicates different phases) in three types of cross-section geometry : (a) equilateral triangle, (b) square and (c) right triangle

three-phase flow simulation on the fluid configuration illustrated in Fig.5(a). The triangle side length is 90 lattice sites. We adjusted the viscosity of the center phase ν_{cen}, while keeping the viscosities of the other two phases to an identical constant value ν_I. Four cases with different viscosity ratios $\nu_I/\nu_{cen} = 1$, $1/3$, $1/5$, and $1/10$ are considered here. The boundary conditions were set as the same with the above validation case. In Fig.6, we plotted velocity profiles along the center line of the cross-sectional triangle for the cases with different viscosity ratios. Indeed, the condition with $\nu_I/\nu_{cen} = 1:1$ is equivalent with the situation of single-phase flow. It can be seen that the velocity of the center phase decreases substantially with the increase of its viscosity. As a result, the low-velocity center phase will drag the layer fluid through the viscous shear force at the interface, which reduces the permeability of the corner phase. These results again demonstrated the importance of the viscous coupling effect. The impact of viscosity variation of the center phase on the corner phase's velocities is relatively small. This is because the shear force from the center phase has to be transmitted through the middle layer phase to the corner phase in this sandwich configuration, and the corner phase's velocities are mainly determined by the non-slip condition of the stationary wall.

3. Results and discussion

In this section, we use the three-phase LBM model as a direct simulator to further examine the impact of the viscous coupling effect on the flow properties inside the pore throats of PNM with various configurations. In PNM, the cross-section of individual pore throats are usually modeled as

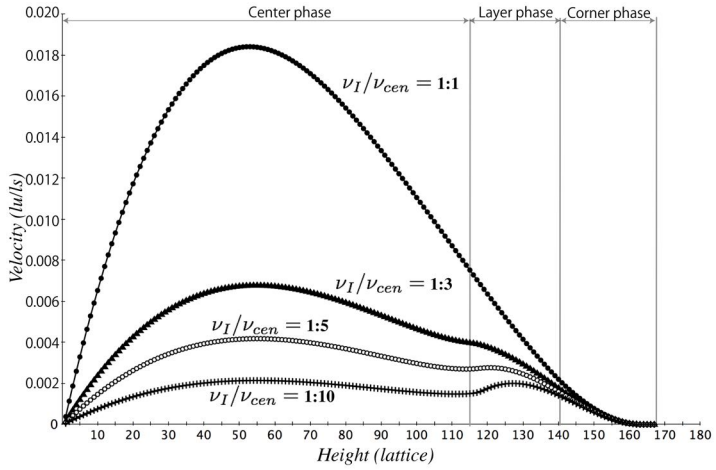

Figure 6: Fluid velocities along the triangle center line with different viscosity ratio conditions ν_I/ν_{cen}

triangles and polygons [46]. Here, in addition to the equilateral triangle, the often-used square and right triangle are also considered in this study. The fluid configuration in a pore/throat corner of these three geometries are illustrated in Fig. 5. The square side length has 190 lattice sites. The right triangle is composed of 30° and 60° angles with the shortest side which has a length of 210 lattice sites. The length of the pore throat along the flow direction is 20 lattice sites. Bounce-back boundary conditions are applied on all the walls, and the periodic boundary conditions are applied on the flow direction. All the simulations used the same pressure gradient meaning the same magnitude of driving force. The driving force is set to be low enough to achieve a small capillary number $\sim 1.0 \times 10^{-4}$ ($\mathrm{Ca} = \mu U/\sigma$, where U denotes the mean velocity), and the direction of interfacial tension force is always orthogonal to the direction of pressure gradient in our scenario. Therefore, the interfaces are very stable in our simulations. The empirical equation (Eq. (6)) indicates that the conductance depends on the parameters such as wettability (contact angle), corner half angle, saturation of each phase (areas), and the viscosity ratios. The corner phase conductance changes under various conditions (combination of different viscosity ratio, contact angles, saturations and fluid configurations) have been studied to quantify those parameters' impacts on viscous coupling effects. The other parameters including density ratio and interfacial tension ratio are set to be unity for simplicity.

3.1. Effect of pore throat geometries

Three geometries (Fig.5) are considered for the shape of cross-section of pore throats. These geometries contain different corner angles. The wettability was set to be neutral for all the cases here, which means the contact angles $\theta_I = \theta_{II} = 90°$. To investigate the viscous coupling effect on the conductance of corner phase, we kept the viscosity of corner phase as a constant while adjusting the viscosities of the layer and center phases with different sets of viscosity ratio ($\nu_{cor} : \nu_{lay} : \nu_{cen} = 1 : 1 : 1 \sim 1 : 10 : 1$ and $\nu_{cor} : \nu_{lay} : \nu_{cen} = 1 : 1 : 1 \sim 1 : 1 : 10$). First, we individually adjusted the viscosity of the layer or center phase while fixing the other two phases' viscosity.

Increase of the viscosity of layer phase leads to a decrease of conductance of the corner phase (red lines in Fig. 7). The same trend can be observed for the results of center phase's viscosity adjustment (yellow lines in Fig. 7). However, for all the cases, the layer phase viscosity change has an obvious larger impact on the corner phase's flow rate compared with the center layer viscosity change (the red curve is always below yellow curve in Fig. 7 and has a steeper gradient). Since the layer phase is adjacent to the corner phase, the shear force change caused by the viscosity increase of the layer phase has a direct impact on the corner phase. For the square geometry, the viscosities of center phase and layer phase have a similar effect (Fig. 7(b)) on the corner phase's conductance. (the difference between the red curve and yellow curve of 90 degree corner of square in Fig. 7(c) is smaller than other cases with small corner angles). On the other hand, it is found that there is no strong influence of center phase's viscosity change on the corner phase's conductance when the corner angle is small (yellow curve is almost horizontal in Fig. 7(c)). The magnitude of the total shear force of center phase transmitting to the corner fluid depends on the area of interface. Larger corner angle results in a wider area of interface. Therefore, the effect of the center phase viscosity is much greater in the 90 degree corner, while it is almost negligible in 30 degree corner. In the case of the 30 degree corner, the ratio of interfacial area to the whole fluid boundary is low, therefore the shear force between center phase and the corner phase has a smaller contribution to the flow rate compared to the wall shear force from the no-slip boundary condition.

We also estimated the flow rate for the conductance of corner phase using the empirical equation (Eq.6). Recall that the parameter f implicitly reflects the viscosity coupling effect between each phase in the empirical equation Eq.6 of the conductivity. The $f \in [0, 1]$ can be seen as a measurement for

slip effect at the interface. $f = 1$ means a no-flow boundary condition, while $f = 0$ means a free-slip boundary condition at the interface. Here, $f = 0$ corresponds to the case with identical viscosity (viscosity ratio equals to 1), while $f = 1$ corresponds to the case with infinite viscosity of layer and center phase (viscosity ratio equals to 0). The possible results of corner phase's flow rate calculated by the conventional empirical equation (Eq.6) with the parameter f treated as a variable in the range of $[0, 1]$ are plotted in Fig.7 as black line. It is seen that the empirical equation underestimated the corner phase conductance for all cases compared with our results of direct simulations. Therefore, the original empirical equation cannot capture the accurate viscous coupling effect.

To further investigate the relationship between the corner phase's conductance and viscosities of the other two phases, we then run 100 simulations by fixing only the corner phase's viscosity and adjusting the viscosity of center together with that of layer phases with various combinations of viscosity ratios $\nu_{cor} : \nu_{lay} : v_{cen} = 1 : 1 : 1 \sim 1 : 10 : 10$. The transition of the corner phase's conductance when increasing the viscosities of the other two phases (Fig.8) shows that the viscous coupling effects of both center and layer phases are significant for geometries with large corner angles (Fig.8 (a) and (b)) while the center phase's viscosity change has only a small impact on the configuration of small corner angle (Fig.8 (c)). The transition of corner phase's conductance shows a difference between the equilateral triangle and right triangle even if the corner angle is the same (Fig.8 (a) and (d)). Therefore the shape of cross-section also has an impact on the viscous coupling effect. A symmetrical cross-section is favorable for the transmission of shear forces. In the case of right triangle, the center phase's viscosity has a smaller influence due to asymmetric shape of cross-section.

3.2. Dependence on contact angle

To investigate the viscous coupling effect under various contact angle conditions, we adjusted the wettability of the solid wall to create three different configurations with different phase contact angles (case I : $\theta_{cl} = 60°$, $\theta_{lb} = 90°$; case II : $\theta_{cl} = 135°$, $\theta_{lb} = 135°$; case III : $\theta_{cl} = 90°$, $\theta_{lb} = 135°$). The subscript cl represents the interface between the corner and layer phase, and lb denotes the interface between the layer and center (bulk) phase. The equilibrium configurations of the three phases with different contact angles are displayed in Fig.9.

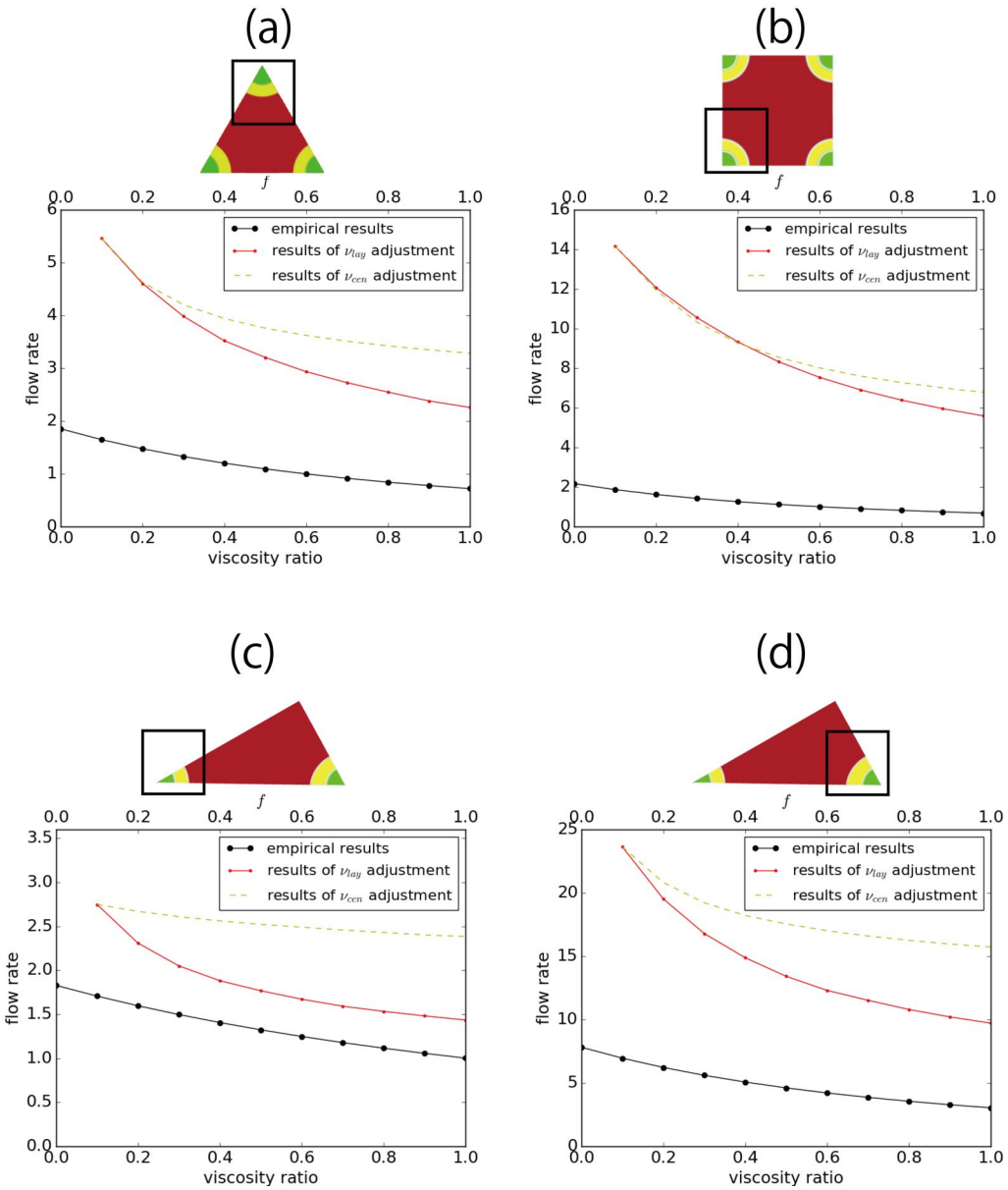

Figure 7: Effect of viscosity ratio on the conductance of corner phase (a) 60 degree corner of equilateral triangle, (b) 90 degree corner of square, (c) 30 degree corner of right triangle and (d) 60 degree corner of right triangle

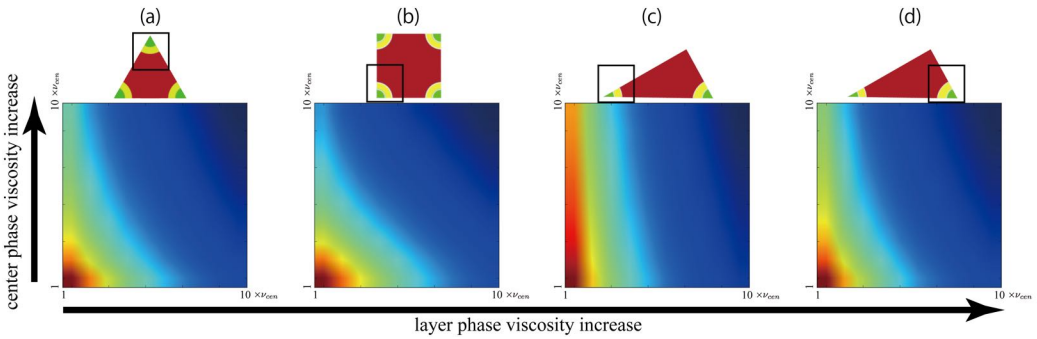

Figure 8: Transition of corner phase's conductance when increasing the viscosities of center phases (y axis) and layer phase(x axis) for different fluid configurations; red color indicates high flow rate and blue color represents the low flow rate

We independently increased the viscosities of layer phase and center phase respectively. The simulated conductances of the corner phase with different sets of viscosity ratio ($\nu_{cor} : \nu_{lay} : v_{cen} = 1 : 1 : 1 \sim 1 : 10 : 1$ and $\nu_{cor} : \nu_{lay} : v_{cen} = 1 : 1 : 1 \sim 1 : 1 : 10$) are shown in Fig. 9. The conductance of corner phase decreases with the increase of the other phases' viscosities due to the viscous coupling effect. The viscosity increase of the layer phase (red lines in Fig.9) has a greater impact on the corner phase's conductance than that of the center phase (yellow lines in Fig.9). These two kinds of trends are consistent with the above observation for the same reason discussed in section 3.1.

Viscous coupling effect arising from center phase viscosity showed dependence on the contact angle. For case III ($\theta_{cl} = 90°$, $\theta_{lb} = 135°$), the center phase viscosity change has a negligible effect on corner phase's conductance, while the conductance of corner phase decreases faster for case I compared with case II and III (yellow curves in Fig.9). In case III, the layer phase forms a biconcave lens shape and the area of the layer phase is smaller compared with case I and II. Such shape results in a lower velocity distribution and therefore lower shear force. On the other hand, the contact angle has little influence when changing the layer phase viscosity (three red curves in Fig.9 almost collapse together). The viscous coupling has to act through the interface, whose effect is directly related to the length of the interface. The lengths of the interface between corner and layer phases are almost the same for three cases. The change of interfacial length caused by the variation of the corner phase's contact angle is limited. As a result, only a very small

impact on the viscous coupling effect can be observed when the contact angle of corner phase changed.

3.3. Dependence on saturation

To investigate the dependence of the viscosity coupling effect on the saturations of the three phases, configurations with thinner thickness layer phase (Fig. 10 (b) case II) and smaller area corner phase (Fig. 10 (c) case III) are constructed based on the original case (Fig.10 (a) case I). The wettability was set to neutral for all the three phases. The saturations of corner phase for the three cases are $S_c^I = S_c^{II} = 0.056$, $S_c^{III} = 0.027$, and the saturations of layer phase for the three cases are $S_L^I = 0.102$, $S_L^{II} = 0.049$, $S_L^{III} = 0.081$. The results again showed that the viscosity change of the layer phase has an obvious larger impact on the conductance of the corner phase (Fig.10). Increase of the ratio $\nu_{lay} : \nu_{cor}$ up to 10 results in a decrease of 50% for the corner phase's conductance, while increasing the ratio $\nu_{cen} : \nu_{cor}$ leads to a decrease of roughly 10%$\sim$20% for the corner phase's conductance. This trend is similar to Fig.9 for the same reason that the shear force from layer directly acts on the corner phase through their shared interface.

The differences of the three curves for different saturation cases are small (Fig. 10). Note that, the absolute conductance (flow rate) in the empirical equation (Eq. 6) is related to the value of saturation. Here, we focused on investigating the viscous coupling effect based on the normalized conductance $\hat{g} = \frac{g_i}{g_b}$ with g_b being the base conductance calculated by using identical viscosity ratio and g_i being the conductance calculated by various viscosity ratios. The results of normalized conductance showed that the saturation variation has a small effect on the viscous coupling. For the cases I and II with the same saturation of corner phase, an increase of the layer phase's saturation leads to a slightly bigger impact of viscous coupling effect from the layer phase. If we further decrease the saturation of the corner phase, the viscous coupling effect from the layer phase becomes stronger. With regard to center phase viscosity adjustment, our results of case II showed the largest viscous coupling effect. Since the shear force from the center phase has to be transmitted across the layer phase, the thinner layer phase shortens the distance between the corner phase and center phase in case II. Therefore, the propagation of the viscous coupling effect from the center phase to corner phase becomes easier.

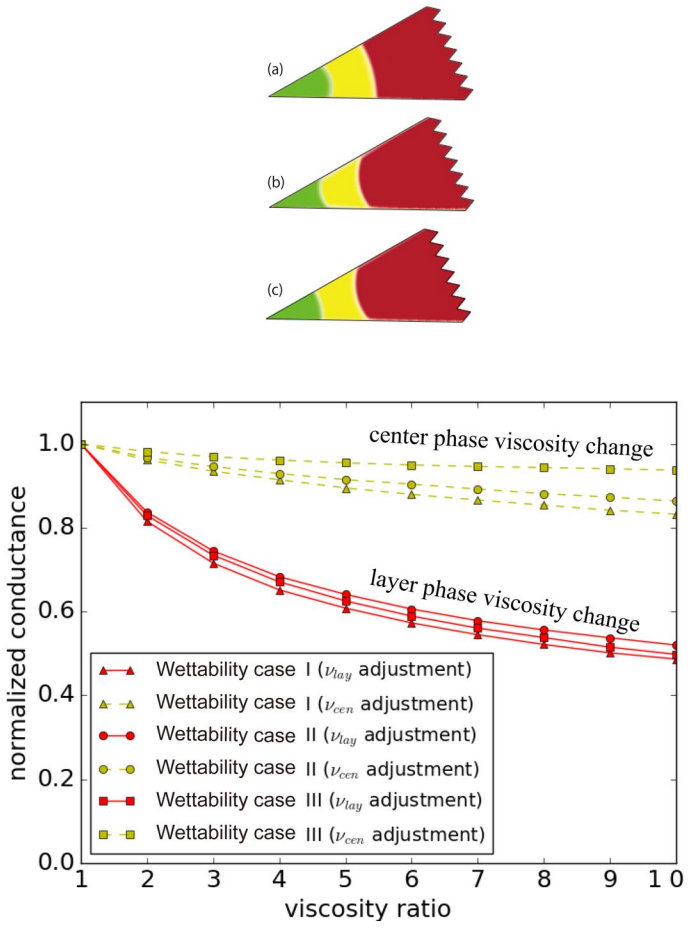

Figure 9: Effect of contact angle on the conductance of corner phase with viscosity changing; Left shows the configurations for different contact angles: case I (a), case II (b) and case III (c);

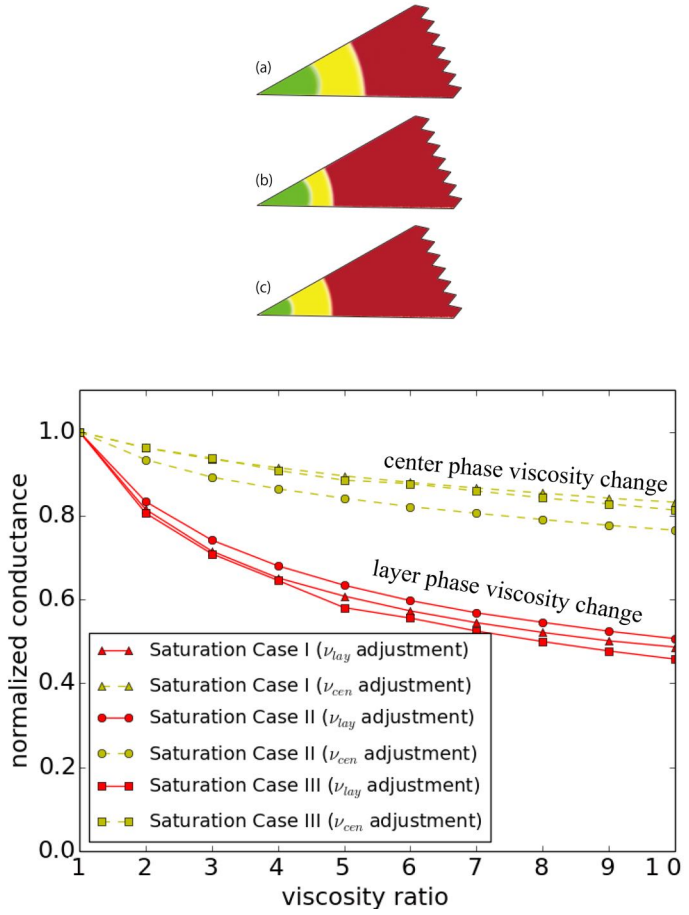

Figure 10: Effect of saturation on the conductance of corner phase with viscosity changing; Left shows the configurations for different saturations: case I (a), case II (b) and case III (c);

3.4. Modification factor

The above results show that the viscous coupling effect on predicting the transport properties is significant. In the original model by Hui and Blunt [11], the empirical equation is unable to match the results of direct simulation with a single constant parameter f which is related to the viscous coupling effect (Fig.8). Here we try to extend the original model by incorporating the viscous coupling effect extracted from the direction simulations and improve the predication accuracy.

The results in section 3.2 and 3.3 indicated that viscous coupling effect was not very sensitive to wettability or saturations, which is agreed with the finding in the reference [16]. The viscosity ratios has the largest impact on the conductance. Therefore, we introduce a new function of the two viscosity ratios $M_1 = \nu_{cor}/\nu_{lay}$ and $M_2 = \nu_{lay}/\nu_{cen}$ to account the viscous coupling effect.

Assuming the parameter f in the empirical equation (Eq.6) to be 0, we defined a reference value of conductance as:

$$g_c^r = \frac{A_c^2 \tan\alpha(1-\sin\alpha)^2\varphi_3^2}{12\mu\sin^2\alpha(1-\varphi_3)} \tag{29}$$

Then we propose a new conductance model by correcting the reference value through a modification factor $f_c^v(M_1, M_2)$ to approach the results of direct simulations.

$$g_c = g_c^r \cdot f_c^v(M_1, M_2) = \frac{A_c^2 \tan\alpha(1-\sin\alpha)^2\varphi_3^2}{12\mu\sin^2\alpha(1-\varphi_3)} \cdot f_c^v(M_1, M_2) \tag{30}$$

To propose an expression for this function, we use second order polynomial model expressed by two variables M_1 and M_2.

$$f_c^v(M_1, M_2) = a^c M_1 + b^c M_2 + c^c M_1 M_2 + d^c M_1^2 + e^c M_2^2 + h^c \tag{31}$$

The six constant parameters $a^c \sim h^c$ are determined by a least-squares algorithm to fit with the data from direct simulations $f_{c,sim}^v = g_{c,sim}/g_c^r$. The obtained parameters are listed in Table.1. The modification factors calculated by Eq.31 using the obtained parameters (surfaces in Fig.11) showing a very good agreement with the simulation results (dots in Fig.11). Therefore, the proposed new conductance model with this modification factor (Eq. 30) is able to capture the viscous coupling effects under different viscosity ratio conditions. Here, the modification factor is considered to be independent to

the wettability and saturation because the viscous coupling effect was not very sensitive to these parameters. The proposed modification factor is indeed a relative ratio between the conductance predicted under three-phase condition with viscous coupling effect and that under single-phase state with free-slip interface condition. The relationship between conductance and wettability as well as saturation is already included in the reference function (Eq. 29). Therefore, the modification factor scales the conductance in a similar manner when the contact angle or saturation changes. This modification factor may show dependence if the contact angle or saturation is extremely high or low. However, for most of values of wettability and saturation, such dependence can be neglected [16].

Based on the same procedure, we propose the modification factor f_l^v for the layer phase's conductance. The base reference value g_l^r for layer phase's conductance without viscous coupling effect is defined from the original equation (Eq.10) with $f_1 = f_2 = 0$:

$$g_l^r = \frac{A_1^3(1-\sin\alpha)^2\tan\alpha\varphi_3^2}{12\mu A_{cl}\sin^2\alpha(1-\varphi_3)\left[1-\sqrt{\frac{A_2}{A_{cl}}}\right]^2} \tag{32}$$

Similarly, the layer phase's conductance can be corrected by the modification factor f_l^v to include viscous coupling effect :

$$g_l = g_l^r \cdot f_l^v(M_3, M_4) \tag{33}$$

where, viscosity ratios are defined as $M_3 = \nu_{cor}/\nu_{lay}$ and $M_4 = \nu_{cen}/\nu_{lay}$. Again, the polynomial type of modification function is used:

$$f_l^v(M_3, M_4) = a^l M_3 + b^l M_4 + c^l M_3 M_4 + d^l M_3^2 + e^l M_4^2 + h^l \tag{34}$$

The six constant parameters $a^l \sim h^l$ obtained by fitting the function to data from direct simulations using least-squares algorithm are shown in Table.2. These modification factors can be used to improve the original pore-network model for a better performance of predicting the transport parameters by incorporating the viscous coupling effect.

3.5. A general data-driven machine learning model for permeability

The above modification factor is proposed as a correction for the original empirical equation for conductance. For a practical application, a data-driven way to predict the multiphases' permeability considering the viscous

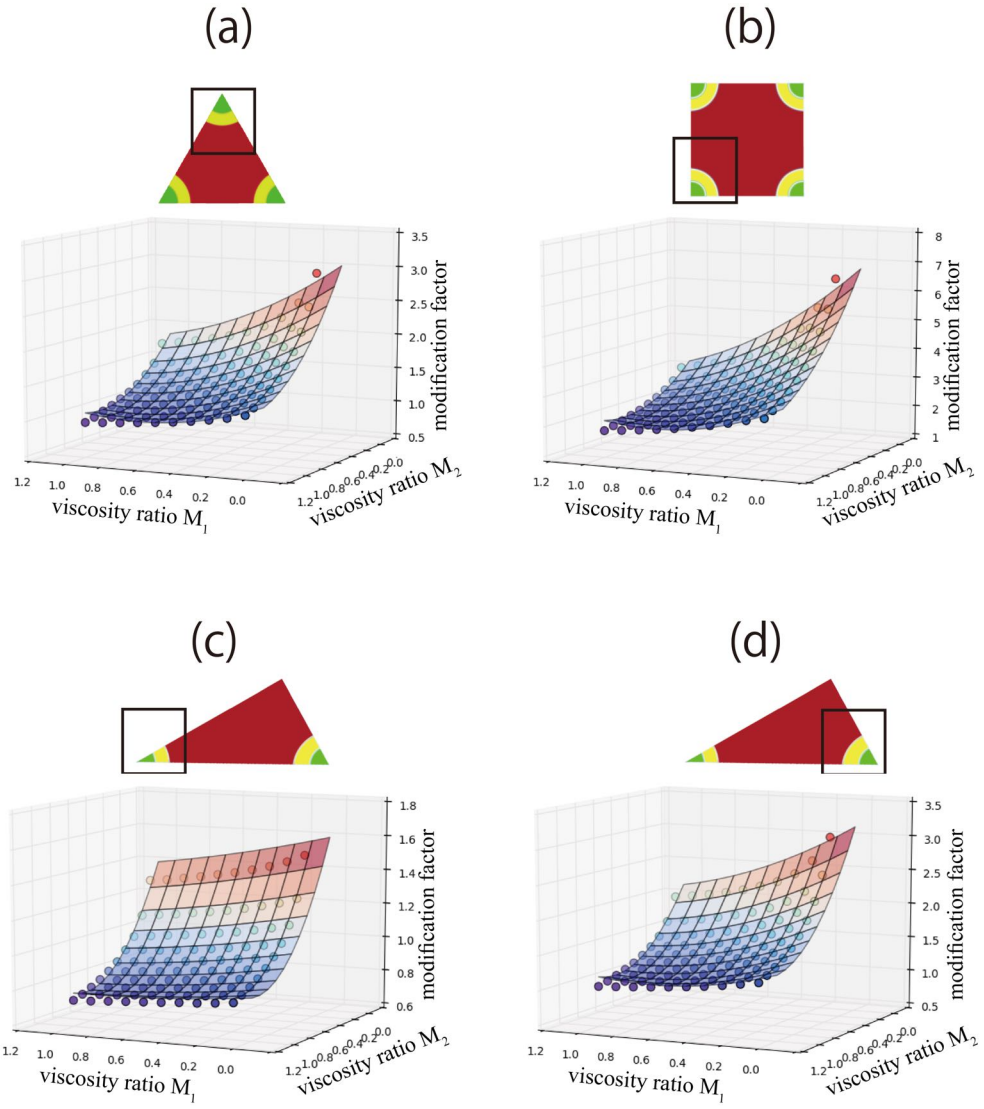

Figure 11: Modification factor f_c^v as a function of viscosity ratios M_1 and M_2 for different geometries and surfaces fit to our direct simulation data in circle dots: red and blue color indicate high and low values respectively

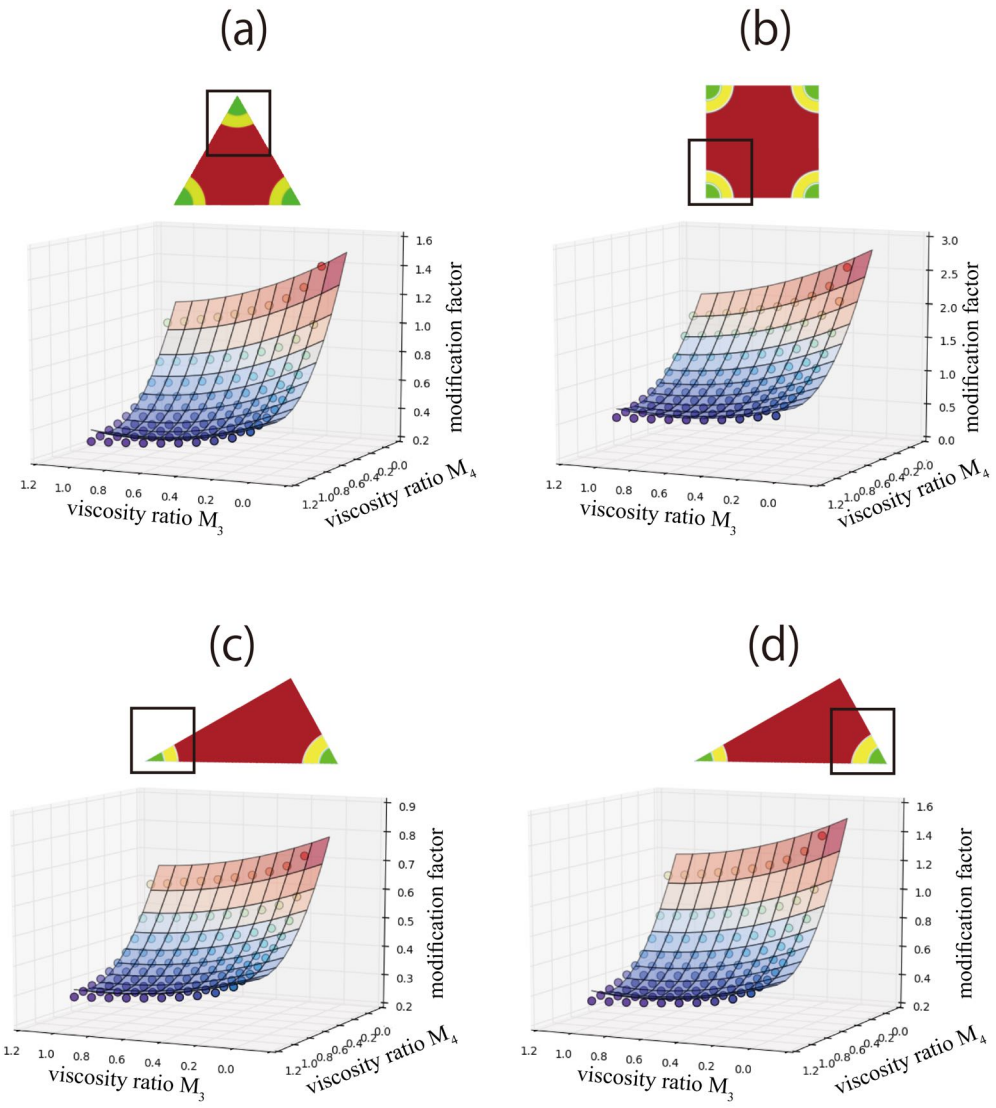

Figure 12: Modification factor f_l^v as a function of viscosity ratios M_1 and M_2 for different geometries and surfaces fit to our direct simulation data in circle dots: red and blue color indicate high and low values respectively

Table 1: Parameters of modification factor function of corner phase's conductance for different fluid configurations

corner	a^c	b^c	c^c	d^c	e^c	h^c
equilateral triangle 60°	3.0431	-1.8606	-2.9031	0.8909	0.7065	1.2060
square 90°	6.8287	-5.4973	-5.9767	2.7358	1.9370	2.0739
right traingle 30°	1.6021	-0.2614	-1.6672	0.1473	0.0634	0.8840
right traingle 60°	3.1593	-1.570	-3.3794	0.7843	0.5753	1.5872

Table 2: Parameters of modification factor function of layer phase's conductance for different fluid configurations

corner	a^l	b^l	c^l	d^l	e^l	h^l
equilateral triangle 60°	1.5041	-0.7247	-2.2332	0.2695	0.3194	1.2433
square 90°	2.8318	-1.3588	-3.9132	0.5868	0.5736	1.9658
right triangle 30°	0.7893	-0.2457	-0.9183	0.0523	0.1152	0.5173
right triangle 60°	1.5044	-0.5770	-2.2305	0.1783	0.2706	1.2676

coupling effect is further proposed. Based on the data obtained from direct simulations, the machine learning method was adopted to develop a fast and accurate model for permeability. Machine learning methods provide a function using a set of neurons and weights to express the relationship between inputs and outputs [58]. Here, the Levenberg-Marquardt algorithm is used as the optimizer to train an artificial neural network (ANN) to predict the permeability (output) based on the properties in terms of three phases' configuration, throat's geometry, viscosity ratios, and etc.(inputs). Levenberg-Marquardt is an iterative algorithm to find the minimum of a loss function taking the form of a sum of squared errors [59, 60]. This algorithm is an efficient tool to optimize weights and biases of a neural network approach in a second-order training speed without having to compute the Hessian matrix [61, 62, 63]. In this study, we adopted a fully-connected neural network with one-hidden-layer (Fig. 13). The optimal size of the hidden layer is usually a prior-unknown variable, therefore two ANN architectures with different number of nodes (ANN1: 6 nodes; ANN2: 7 nodes) in the hidden layer were considered here. Both ANNs have 8 input parameters and one output of the permeability.

We considered 8 input parameters which include corner angle α, contact

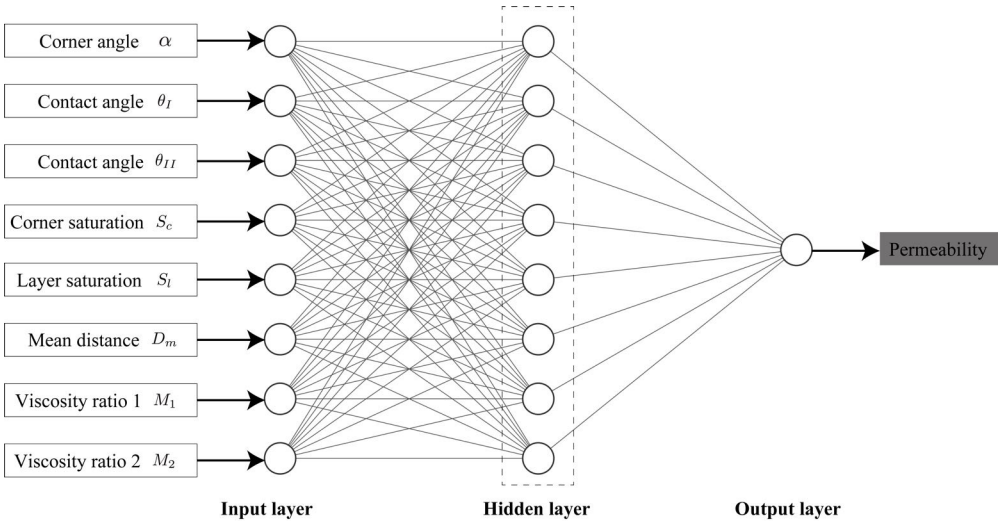

Figure 13: Illustration of the ANN for machine learning to model the permeability with 8 input parameters

angle between corner and layer phases θ_I, contact angle between layer and center phases θ_{II}, mean distance D_m of the cross area's shape, saturation of corner phase S_c, saturation of layer phase S_l, viscosity ratio M_1, and viscosity ratio M_2 (Fig. 13). Here the mean distance D_m is obtained by calculating the average of the Euclidean distance map of the pixel-based cross section [63]. The Euclidean distance of a void space means the distance from the void pixel to the nearest solid pixel. The mean distance parameter was adopted here because it reflects the topological feature of cross section's shape and is highly correlated with the permeability [63] and the above modification factor also showed a heavy dependence on the shape of cross section. Training of this neural network was conducted by using the *nftool* function in *Deep Learning Toolbox* of MATLAB. To train the neural networks, we built a database composed of 3200 entries using different combinations of input parameters presented in Section 3.1-3.3 for various situations. We take 70% of them for training, 15% for validation and 15% for testing. Then the mean squared error (MSE) and coefficient of determination (R^2) are calculated to evaluate the training performance.

Fig. 14 and 15 showed the relationships between the original data from direction simulations and predicted results by the ANNs for the permeabilities of corner phase and layer phase, respectively. The results of ANN1 with

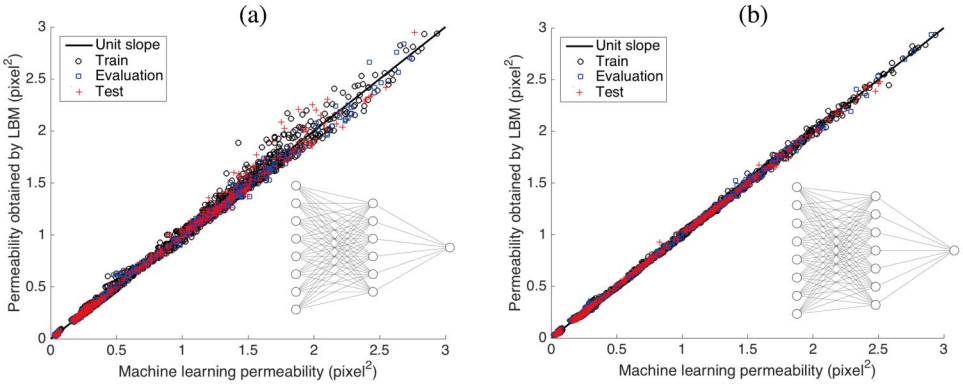

Figure 14: The capability of ANN to predict the permeability of corner phase including training, evaluation and testing data, (a) ANN1 with 6-node hidden layer, (b) ANN2 with 7-node hidden layer.

Table 3: Learning performance for corner phase's permeability of the two ANNs in terms of coefficient of determination (R^2) and mean squared error (MSE).

Data set	ANN1 MSE	ANN1 R^2	ANN2 MSE	ANN2 R^2
Training	1.76111e-3	9.976630-1	2.05180e-4	9.99730e-1
Validating	1.37162e-3	9.98434e-1	2.66466e-4	9.99649e-1
Testing	2.77962e-3	9.96594e-1	2.90566e-4	9.99645e-1

6-node hidden layer is more scattered than that of the ANN2 with 7-node hidden layer. The learning performance of ANN1 and ANN2 are provided in Table.3 in terms of mean squared error (MSE) and coefficient of determination (R^2). These results quantitively demonstrated a better prediction performance of ANN2. The ANN2 with 7-node hidden layer is able to perfectly calculate the permeability of multiphase flow in pore throat with the given 8 input parameter. Further increasing the size of hidden layer may lead to over-fitting. Therefore, the optimized size of the hidden layer must be 7 nodes for our proposed neural network model. Finally an explicit function (in supplementary material) can be extracted from this trained neural network and then coupled into the PNM to improve the accuracy of permeability calculation by incorporating the advantages of direct simulations with the viscous coupling effect.

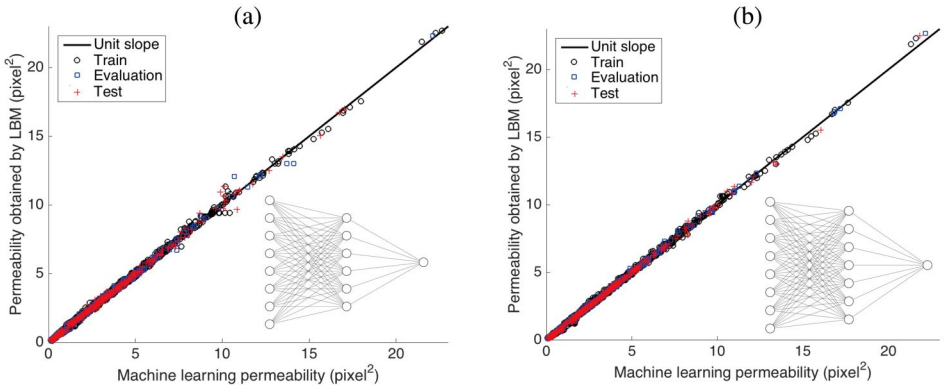

Figure 15: The capability of ANN to predict the permeability of layer phase including training, evaluation and testing data, (a) ANN1 with 6-node hidden layer, (b) ANN2 with 7-node hidden layer.

Table 4: Learning performance for layer phase's permeability of the two ANNs in terms of coefficient of determination (R^2) and mean squared error (MSE).

Data set	ANN1 MSE	ANN1 R^2	ANN2 MSE	ANN2 R^2
Training	1.07605e-2	9.99245e-1	7.76235e-3	9.99407e-1
Validating	1.67436e-2	9.98678e-1	1.05380e-2	9.99437e-1
Testing	2.02200e-2	9.98578e-1	1.08309e-2	9.99271e-1

4. Conclusion

In this study, the viscous coupling effects in three-phase flow through pore throat channels have been studied by using the multiphase LBM direct simulation under various conditions with different saturations, wettability, and fluid configurations. The results indicate that the viscous coupling effect during simultaneous flow of different fluid phases has a significant impact on the hydraulic conductance of fluid layers occupying the corner areas. This viscous coupling effect is heavily correlated to the shape of cross-section and the length of interface across which the momentum transfers. Our direct simulation results show that the geometric parameters such as corner angle and the viscosity ratios largely affect the viscous coupling effects. We have also demonstrated that the conventional empirical equation derived using free-slip and no-flow boundary fails to capture the correct conductance for a range of viscosity ratios. A modification factor which is expressed as a function of viscosity ratios is proposed to correct the original empirical equation to include the viscous coupling effect. With this modification factor, the results calculated by the corrected equation agree well with the data from direct simulations.

We further proposed a more elegant way to predict the permeability of three-phase flow in pore throat tubes by using the machine learning method. Two ANNs with different nodes of hidden layer were trained by a database built from the results of direct simulations using different combinations of 8 inputs including various geometric parameters, wettability and viscosity ratios. The results showed that the ANN with 7-node hidden layer provide a perfect capability of estimating the permeabilities with coefficient of determination (R^2) higher than 0.99.

These two proposed new models can be directly incorporated into pore network modeling for predicting flow transport properties with the viscous coupling effect for large core-scale model. Though the present study only considered the straight pore-throat tubes, our approach can be easily extended to deal with more complicated shape of pore throats. The coupling of direction simulation and pore-network modeling through this way has a great potential to improve the accuracy of pore-network modeling by incorporating more detailed pore-scale information while still maintaining good computational efficiency.

5. Acknowledgements

This work was supported by JSPS through a Grant-in-Aid for Young Scientists (Grant No. 19K15100).

6. Supplementary material

The training data are provided and the trained neural networks are given as explicit functions in the repository:
https://github.com/fjiang-cloud/viscousCouple.

[1] M. J. Blunt, B. Bijeljic, H. Dong, O. Gharbi, S. Iglauer, P. Mostaghimi, A. Paluszny, C. Pentland, Pore-scale imaging and modelling, Advances in Water Resources 51 (2013) 197–216.

[2] S. Bryant, M. Blunt, Prediction of relative permeability in simple porous media, Physical review A 46 (4) (1992) 2004.

[3] V. Joekar-Niasar, S. Hassanizadeh, Analysis of fundamentals of two-phase flow in porous media using dynamic pore-network models: A review, Critical reviews in environmental science and technology 42 (18) (2012) 1895–1976.

[4] I. FATT, The network model of porous media. i. capillary pressure characteristics., Petrol. Trans. AIME 207 (1956) 144–159.

[5] A. Raoof, S. Hassanizadeh, A new formulation for pore-network modeling of two-phase flow, Water Resources Research 48 (1) (2012).

[6] M. J. Blunt, Flow in porous media pore network models and multiphase flow, Current opinion in colloid & interface science 6 (3) (2001) 197–207.

[7] S. Bakke, P.-E. Øren, et al., 3-d pore-scale modelling of sandstones and flow simulations in the pore networks, Spe Journal 2 (02) (1997) 136–149.

[8] H. Dong, M. J. Blunt, Pore-network extraction from micro-computerized-tomography images, Physical review E 80 (3) (2009) 036307.

[9] T. W. Patzek, et al., Verification of a complete pore network simulator of drainage and imbibition, in: SPE/DOE Improved Oil Recovery Symposium, Society of Petroleum Engineers, 2000.

[10] D. H. Fenwick, M. J. Blunt, et al., Network modeling of three-phase flow in porous media, SPE Journal 3 (01) (1998) 86–96.

[11] M.-H. Hui, M. J. Blunt, Effects of wettability on three-phase flow in porous media, The Journal of Physical Chemistry B 104 (16) (2000) 3833–3845.

[12] M. Piri, M. J. Blunt, Three-dimensional mixed-wet random pore-scale network modeling of two-and three-phase flow in porous media. i. model description, Physical Review E 71 (2) (2005) 026301.

[13] V. S. Suicmez, M. Piri, M. J. Blunt, et al., Pore-scale modeling of three-phase wag injection: Prediction of relative permeabilities and trapping for different displacement cycles, in: SPE/DOE Symposium on Improved Oil Recovery, Society of Petroleum Engineers, 2006.

[14] A. R. Al-Dhahli, S. Geiger, M. I. van Dijke, et al., Three-phase pore-network modeling for reservoirs with arbitrary wettability, SPE journal 18 (02) (2012) 285–295.

[15] P. H. Valvatne, M. J. Blunt, Predictive pore-scale modeling of two-phase flow in mixed wet media, Water Resources Research 40 (7) (2004).

[16] C. Xie, A. Q. Raeini, Y. Wang, M. J. Blunt, M. Wang, An improved pore-network model including viscous coupling effects using direct simulation by the lattice boltzmann method, Advances in water resources 100 (2017) 26–34.

[17] M. Shams, A. Q. Raeini, M. J. Blunt, B. Bijeljic, A study to investigate viscous coupling effects on the hydraulic conductance of fluid layers in two-phase flow at the pore level, Journal of colloid and interface science 522 (2018) 299–310.

[18] R. Ehrlich, Viscous coupling in two-phase flow in porous media and its effect on relative permeabilities, Transport in Porous Media 11 (3) (1993) 201–218.

[19] H. Dehghanpour, B. Aminzadeh, M. Mirzaei, D. DiCarlo, Flow coupling during three-phase gravity drainage, Physical Review E 83 (6) (2011) 065302.

[20] H. Dehghanpour, B. Aminzadeh, D. DiCarlo, Hydraulic conductance and viscous coupling of three-phase layers in angular capillaries, Physical Review E 83 (6) (2011) 066320.

[21] L. Yang, J. Yang, E. Boek, M. Sakai, C. Pain, Image-based simulations of absolute permeability with massively parallel pseudo-compressible stabilised finite element solver, Computational Geosciences 23 (5) (2019) 881–893.

[22] J. A. White, R. I. Borja, J. T. Fredrich, Calculating the effective permeability of sandstone with multiscale lattice boltzmann/finite element simulations, Acta Geotechnica 1 (4) (2006) 195–209.

[23] A. Q. Raeini, M. J. Blunt, B. Bijeljic, Modelling two-phase flow in porous media at the pore scale using the volume-of-fluid method, Journal of Computational Physics 231 (17) (2012) 5653–5668.

[24] A. Q. Raeini, M. J. Blunt, B. Bijeljic, Direct simulations of two-phase flow on micro-ct images of porous media and upscaling of pore-scale forces, Advances in water resources 74 (2014) 116–126.

[25] A. Q. Raeini, B. Bijeljic, M. J. Blunt, Modelling capillary trapping using finite-volume simulation of two-phase flow directly on micro-ct images, Advances in Water Resources 83 (2015) 102–110.

[26] E. S. Boek, M. Venturoli, Lattice-boltzmann studies of fluid flow in porous media with realistic rock geometries, Computers & Mathematics with Applications 59 (7) (2010) 2305–2314.

[27] F. Jiang, T. Tsuji, Impact of interfacial tension on residual co2 clusters in porous sandstone, Water Resources Research 51 (3) (2015) 1710–1722.

[28] T. Tsuji, F. Jiang, K. T. Christensen, Characterization of immiscible fluid displacement processes with various capillary numbers and viscosity ratios in 3d natural sandstone, Advances in Water Resources 95 (2016) 3–15.

[29] F. Jiang, T. Tsuji, Estimation of three-phase relative permeability by simulating fluid dynamics directly on rock-microstructure images, Water Resources Research 53 (1) (2017) 11–32.

[30] S. Shah, J. Crawshaw, F. Gray, J. Yang, E. Boek, Convex hull approach for determining rock representative elementary volume for multiple petrophysical parameters using pore-scale imaging and lattice–boltzmann modelling, Advances in water resources 104 (2017) 65–75.

[31] I. Zacharoudiou, E. M. Chapman, E. S. Boek, J. P. Crawshaw, Pore-filling events in single junction micro-models with corresponding lattice boltzmann simulations, Journal of Fluid Mechanics 824 (2017) 550–573.

[32] A. Fakhari, Y. Li, D. Bolster, K. T. Christensen, A phase-field lattice boltzmann model for simulating multiphase flows in porous media: Application and comparison to experiments of co2 sequestration at pore scale, Advances in water resources 114 (2018) 119–134.

[33] S. Saito, Y. Abe, K. Koyama, Lattice boltzmann modeling and simulation of liquid jet breakup, Physical Review E 96 (1) (2017) 013317.

[34] S. Saito, A. De Rosis, A. Festuccia, A. Kaneko, Y. Abe, K. Koyama, Color-gradient lattice boltzmann model with nonorthogonal central moments: Hydrodynamic melt-jet breakup simulations, Physical Review E 98 (1) (2018) 013305.

[35] S. Leclaire, A. Parmigiani, O. Malaspinas, B. Chopard, J. Latt, Generalized three-dimensional lattice boltzmann color-gradient method for immiscible two-phase pore-scale imbibition and drainage in porous media, Physical Review E 95 (3) (2017) 033306.

[36] H. Huang, X.-y. Lu, Relative permeabilities and coupling effects in steady-state gas-liquid flow in porous media: A lattice boltzmann study, Physics of Fluids 21 (9) (2009) 092104.

[37] H. Liu, A. J. Valocchi, C. Werth, Q. Kang, M. Oostrom, Pore-scale simulation of liquid co2 displacement of water using a two-phase lattice boltzmann model, Advances in Water Resources 73 (2014) 144–158.

[38] H. Liu, Q. Kang, C. R. Leonardi, S. Schmieschek, A. Narváez, B. D. Jones, J. R. Williams, A. J. Valocchi, J. Harting, Multiphase lattice

boltzmann simulations for porous media applications, Computational Geosciences 20 (4) (2016) 777–805.

[39] I. Zacharoudiou, E. S. Boek, Capillary filling and haines jump dynamics using free energy lattice boltzmann simulations, Advances in water resources 92 (2016) 43–56.

[40] Y. Chen, Y. Li, A. J. Valocchi, K. T. Christensen, Lattice boltzmann simulations of liquid co2 displacing water in a 2d heterogeneous micromodel at reservoir pressure conditions, Journal of contaminant hydrology 212 (2018) 14–27.

[41] J. Wang, X. Zhang, A. G. Bengough, J. W. Crawford, Domain-decomposition method for parallel lattice boltzmann simulation of incompressible flow in porous media, Physical Review E 72 (1) (2005) 016706.

[42] J. Gao, H. Xing, V. Rudolph, Q. Li, S. D. Golding, Parallel lattice boltzmann computing and applications in core sample feature evaluation, Transport in Porous Media 107 (1) (2015) 65–77.

[43] Y. Chen, A. J. Valocchi, Q. Kang, H. S. Viswanathan, Inertial effects during the process of supercritical co2 displacing brine in a sandstone: Lattice boltzmann simulations based on the continuum-surface-force and geometrical wetting models, Water Resources Research (2019).

[44] H. Li, C. Pan, C. T. Miller, Pore-scale investigation of viscous coupling effects for two-phase flow in porous media, Physical Review E 72 (2) (2005) 026705.

[45] A. Al-Futaisi, T. W. Patzek, et al., Three-phase hydraulic conductances in angular capillaries, in: SPE/DOE Improved Oil Recovery Symposium, Society of Petroleum Engineers, 2002.

[46] M. Piri, Pore-scale modelling of three-phase flow, Imperial College (2003).

[47] S. Leclaire, M. Reggio, J.-Y. Trépanier, Progress and investigation on lattice boltzmann modeling of multiple immiscible fluids or components with variable density and viscosity ratios, Journal of Computational Physics 246 (2013) 318–342.

[48] C. Pan, L.-S. Luo, C. T. Miller, An evaluation of lattice boltzmann schemes for porous medium flow simulation, Computers & fluids 35 (8-9) (2006) 898–909.

[49] D. d'Humieres, Generalized lattice-boltzmann equations, Rarefied gas dynamics (1992).

[50] J. Tölke, Lattice boltzmann simulations of binary fluid flow through porous media, Philosophical Transactions of the Royal Society of London. Series A: Mathematical, Physical and Engineering Sciences 360 (1792) (2002) 535–545.

[51] T. Reis, T. N. Phillips, Lattice boltzmann model for simulating immiscible two-phase flows, Journal of Physics A: Mathematical and Theoretical 40 (14) (2007) 4033.

[52] Y. Kuwata, K. Suga, Large eddy simulations of pore-scale turbulent flows in porous media by the lattice boltzmann method, International Journal of Heat and Fluid Flow 55 (2015) 143–157.

[53] H. Liu, A. J. Valocchi, Q. Kang, Three-dimensional lattice boltzmann model for immiscible two-phase flow simulations, Physical Review E 85 (4) (2012) 046309.

[54] S. Leclaire, M. Reggio, J.-Y. Trépanier, Isotropic color gradient for simulating very high-density ratios with a two-phase flow lattice boltzmann model, Computers & Fluids 48 (1) (2011) 98–112.

[55] S. Leclaire, M. Reggio, J.-Y. Trépanier, Numerical evaluation of two recoloring operators for an immiscible two-phase flow lattice boltzmann model, Applied Mathematical Modelling 36 (5) (2012) 2237–2252.

[56] M. Latva-Kokko, D. H. Rothman, Diffusion properties of gradient-based lattice boltzmann models of immiscible fluids, Physical Review E 71 (5) (2005) 056702.

[57] J. Yang, E. S. Boek, A comparison study of multi-component lattice boltzmann models for flow in porous media applications, Computers & Mathematics with Applications 65 (6) (2013) 882–890.

[58] E. Alpaydin, Introduction to machine learning, MIT press, 2014.

[59] D. W. Marquardt, An algorithm for least-squares estimation of nonlinear parameters, Journal of the society for Industrial and Applied Mathematics 11 (2) (1963) 431–441.

[60] M. I. Lourakis, et al., A brief description of the levenberg-marquardt algorithm implemented by levmar, Foundation of Research and Technology 4 (1) (2005) 1–6.

[61] T. Hagan Martin, B. Menhaj Mohammad, Training feed forward networks with the marquardt algorithm, IEEE Trans Neural Netw 5 (6) (1994) 989–993.

[62] H. Yu, B. M. Wilamowski, Levenberg-marquardt training, Industrial electronics handbook 5 (12) (2011) 1.

[63] A. Rabbani, M. Babaei, Hybrid pore-network and lattice-boltzmann permeability modelling accelerated by machine learning, Advances in Water Resources 126 (2019) 116–128.